INSTITUTE OF PHYSICS PUBLISHING PLASMA SOURCES SCIENCE AND TECHNOLOGY

Plasma Sources Sci. Technol. **10** (2001) 395–405 PII: S0963-0252(01)24935-4

Scaling laws for electromagnetic pulsed plasma thrusters

J K Ziemer[1] **and E Y Choueiri**

Electric Propulsion and Plasma Dynamics Laboratory (EPPDyL), Applied Physics Group, Mechanical and Aerospace Engineering Department, Princeton University, Princeton, NJ 08544, USA

Received 23 March 2001, in final form 7 May 2001
Published 5 June 2001
Online at stacks.iop.org/PSST/10/395

Abstract

The scaling laws of pulsed plasma thrusters operating in the predominantly electromagnetic acceleration mode (EM-PPT) are investigated theoretically and experimentally using gas-fed pulsed plasma thrusters. A fundamental characteristic velocity that depends on the inductance per unit length and the square root of the capacitance to the initial inductance ratio is identified. An analytical model of the discharge current predicts scaling laws in which the propulsive efficiency is proportional to the EM-PPT performance scaling number, defined here as the ratio of the exhaust velocity to the EM-PPT characteristic velocity. The importance of the effective plasma resistance in improving the propulsive performance is shown. To test the validity of the predicted scaling relations, the performance of two gas-fed pulsed plasma thruster designs (one with coaxial electrodes and the other with parallel-plate electrodes), was measured under 70 different operating conditions using an argon plasma. The measurements demonstrate that the impulse bit scales linearly with the integral of the square of the discharge current as expected for an electromagnetic accelerator. The measured performance scaling is shown to be in good agreement with the theoretically predicted scaling. Normalizing the exhaust velocity and the impulse-to-energy ratio by the EM-PPT characteristic velocity collapses almost all the measured data onto single curves that uphold the general validity of these scaling laws.

This paper is dedicated to the memory of Dr Daniel Birx

1. Introduction

Pulsed plasma thrusters (PPTs) are high specific impulse (>1000 s) unsteady plasma devices that accelerate an ionized gas to high exhaust velocities and provide impulses useful for many spacecraft manoeuvres, especially satellite attitude control and station keeping [1]. A common version of the PPT, the ablative pulsed plasma thruster (APPT), uses a solid propellant (most typically Teflon) which is ablated by the discharge itself to provide the working gas [2]. While the nature of the acceleration mechanism in the APPT is not entirely clear, it is less ambiguous in gas-fed pulsed plasma thrusters (GFPPTs). GFPPTs can be easily made to operate in an overwhelmingly electromagnetic mode [3]. In this mode the gas is effectively accelerated to a few tens of kilometres per second by a plasma current sheet (produced through the discharge of a capacitor in series with the electrodes), travelling downstream under the action of a Lorentz force due to the interaction of the current in the sheet with the self-induced magnetic field as shown in figure 1. The entire process lasts for 2–20 μs, involves discharge energies between 1 and 100 J, and instantaneous current through the plasma of tens of kiloamps. The resulting impulse per discharge can vary between a few micronewtons and a few millinewtons depending on the values of the discharge energy and injected mass bit.

GFPPTs are now being considered as a potential option for many station-keeping and primary propulsion missions. The benefits of GFPPTs include specific impulse values as large as 10 000 s, arbitrarily low steady-state power requirements,

[1] Present address: Advanced Propulsion Technology Group, NASA Jet Propulsion Laboratory, M/S 125-109, 4800 Oak Grove Drive, Pasadena, CA 91109-8099, USA.

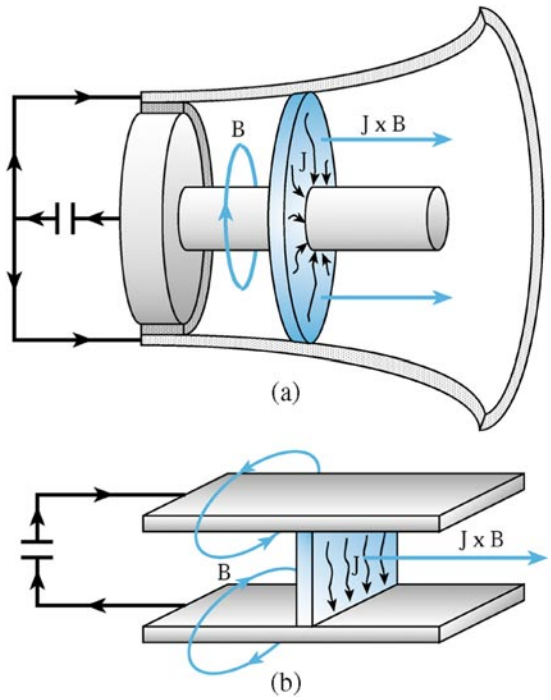

Figure 1. Schematic diagram of (a) coaxial and (b) parallel-plate GFPPTs.

easily throttled thrust, small impulse bits for fine pointing, and the capability to use a large variety of propellants. With inert gases as propellant, the exhaust of a GFPPT is less problematic from a contamination point of view then the carbon-rich exhaust of an ablative (Teflon) PPT. For these reasons, GFPPTs may fill the requirements of many potential missions, including NASA's Europa Orbiter [4], Pluto Fly-by [5] and Space Interferometer missions [6], as well as DARPA's Orbital Express, and Motorola's Teledesic Constellation.

With the present focus on power-limited spacecraft, there is a need for an experimentally verified set of performance scaling relations for low-energy GFPPTs. For the scaling laws to be useful, they should be simple and apply over a wide range of operating conditions and electrode configurations. They should also contain the main character of the acceleration physics while maintaining a good degree of accuracy so that they can be extended to low- (or high-) energy applications.

A number of previous attempts at deriving scaling laws were made in the 1960s (see, for example, [7, 8]) and a number of performance studies on various thruster designs were conducted (see, for example, [9, 10]). However, possibly because of the complex nature of the plasma acceleration in GFPPTs and the multitude of concurrent design changes at the time, the models did not explicitly describe the performance scaling found in experimental measurements.

More recently a series of GFPPTs were developed and studied with the goal of revealing some of the fundamental performance scaling laws of electromagnetic pulsed plasma thrusters (EM-PPTs) [3, 11–14]. Using modern solid-state pulse forming technology to group a series of low-energy (<10 J) pulses together in bursts, we were able to maintain the propellant mass utilization efficiency near 100% while eliminating the need for an ultra-fast valve with exceptional lifetime characteristics. The solid-state nature of the power conditioner also permits the system to be more compact and reliable than the previous single-pulse designs. In addition, the modular nature of the GFPPTs themselves has allowed testing of multiple iterations to examine the effects of changing various design parameters on performance. Simply stated, our goals concerning GFPPT performance scaling have been to:

- derive universal scaling laws for EM-PPT performance,
- experimentally verify the validity and extent of applicability of these laws using GFPPTs,
- obtain physical insight into the basic mechanisms that impact the performance of GFPPTs,
- extend the understanding of how to build higher-performance devices and how to scale them to low (or high) energies while maintaining their high performance.

This paper describes the final results of our performance scaling studies, including both modelling and performance measurements of two GFPPT designs. First, the analytical model will be developed and the GFPPT characteristic velocity and the performance scaling number will be defined. Next, the performance measurements from two GFPPT designs with varying geometry, capacitance, energy, and mass bit will be presented. Finally, the thrust performance and terminal characteristic measurements will be presented in terms of the GFPPT characteristic velocity and the performance scaling number in order to check the validity of the model.

The scaling relations developed in this paper and verified with experiments using GFPPTs should, in principle, apply to any PPT (including APPTs) when operated in a mostly electromagnetic acceleration mode. While we have not experimentally studied the scaling of APPTs (which typically have a significant electrothermal acceleration component), it is relevant to point out that, under some operating conditions, they can be made to operate in an overwhelmingly electromagnetic acceleration mode [15].

2. Derivation of performance scaling relations

As is well known in PPT research, an effective circuit model, in which the current sheet in the plasma acts as a moving element, can offer much insight into the discharge dynamics. Depending on the capacitance C, initial inductance L_0, inductance-per-unit-length L', total resistance (including both the hardware and the effective plasma resistance) R, discharge energy E, and the mass loading (shown schematically in figure 2), the discharge current has a damped oscillatory response with varying character: underdamped, critically damped, or overdamped. The circuit model is usually combined with a 'snowplough' model for mass accumulation in front of the plasma current sheet and numerically integrated to provide a solution that predicts performance under one operating condition. This general technique has been used by us [13] and others [7, 8, 10, 16] to study the behaviour of these plasma devices and span their possible operating conditions. Discovering analytical performance scaling relations from the numerical solutions of these nonlinear differential equations, however, has proven difficult. Some have assumed a fixed inductance and a constant mass [17] or a slightly increasing mass from electrode erosion [18] to decouple the equations and provide analytical solutions. The scaling relations produced

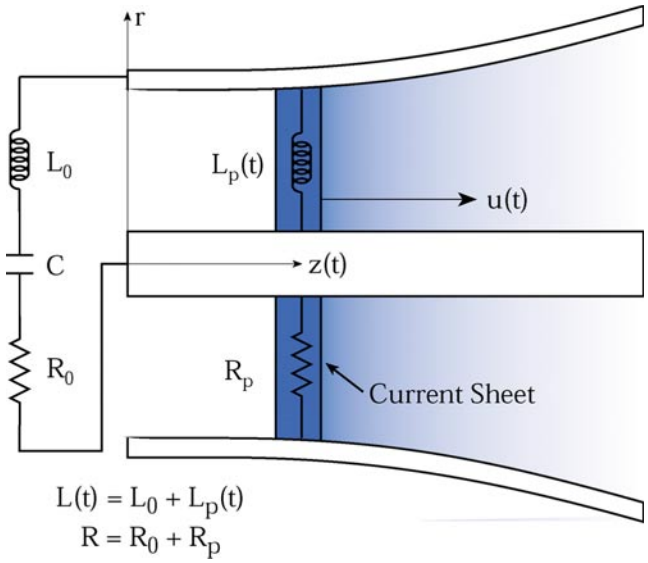

Figure 2. Schematic diagram of a GFPPT discharge, including elements used for the circuit model.

by these techniques, however, only apply to a limited case of GFPPTs where the initial inductance and mass dominate the circuit response.

For the modern GFPPTs we studied, the current waveform is essentially critically damped due to the low inductance (<10 nH) and large capacitance (>100 μF) of the energy storage bank. For the thrusters in this study we experimentally observed that the current waveforms measured with higher mass bits have a slight underdamped quality while lower mass bits can lead to slightly overdamped waveforms. As will be shown, this justifiable assumption of critical damping allows us to relax the assumptions of fixed inductance and mass used in [17, 18] and derive useful, analytical scaling relations for a more realistic model.

We start by expanding Kirchhoff's equation for the effective discharge circuit,

$$V_0 = \frac{1}{C}\int_0^t J\,\mathrm{d}t^* + (R + \dot{L})J + L\dot{J} \tag{1}$$

where V_0 is the initial voltage on the capacitor and J is the total current flowing through the circuit. Solutions to this equation yield current waveforms, $J(t)$, with a character that depends on the changing inductance due to the motion of the current sheet. The total inductance at any given time is related to the position of the current sheet,

$$L = L'z + L_0 \tag{2}$$

where z is the location of the current sheet down the length of the electrodes and the value of L' depends on the electrode geometry. The momentum equation includes the self-induced Lorentz force in the axial direction,

$$\frac{\mathrm{d}}{\mathrm{d}t}(mu) = \frac{1}{2}L'J^2 \tag{3}$$

where m is the instantaneous mass contained in the current sheet moving at a velocity u.

Next, we split the discharge waveform into two segments: before the peak current is reached at $t = t_{peak}$ and from that time until the current reaches zero, $t = t_{final}$. During each segment, we will assume that the current is *linearly* proportional to time. At the beginning of each segment, the values of $L(t)$, $V(t)$, R, and C will be used to determine the slope of the current waveform for the entire segment.

In the first segment, the slope of the current waveform is determined by the initial values of the inductance, L_0, and voltage, V_0, along with the fixed values of capacitance, C, and resistance, R. With these assumptions, the solution to equation (1) with fixed elements has been given in [7] as

$$J = \frac{V_0}{\omega L_0}\,\mathrm{e}^{-(R/2L_0)t}\sin(\omega t) \tag{4}$$

where the natural frequency, ω is

$$\omega = \sqrt{\frac{1}{L_0C} - \frac{R^2}{4L_0^2}} = \sqrt{\frac{1-\psi^2}{L_0C}} \tag{5}$$

and where we have introduced, ψ, the 'critical resistance ratio':

$$\psi \equiv \frac{R}{2}\sqrt{\frac{C}{L_0}}. \tag{6}$$

For ψ near unity the waveform is considered critically damped and for $\psi > 1$ it is overdamped. An underdamped waveform incurs the risk of producing an undesirable secondary breakdown at the breech of the thruster when the current reverses. To avoid this the capacitance must equal or exceed the critical value $4L_0/R_0^2$. Modern PPTs, such as those considered in this study, have initial inductances as low as a few nanohenrys leading to a requirement of only a few hundred microfarads for a critically damped waveform. As already mentioned, for the thrusters in this study, the observed waveforms (e.g. figure 4, below) can be considered critically damped. Consequently we focus on ψ values near unity.

The peak current and the time at which it occurs can be found from this solution in terms of ψ,

$$J_{peak} = V_0\sqrt{\frac{C}{L_0}}\,f_J(\psi) \tag{7}$$

$$f_J(\psi) \equiv \exp\left[-\left(\frac{\psi}{\sqrt{1-\psi^2}}\sin^{-1}(\sqrt{1-\psi^2})\right)\right] \tag{8}$$

$$t_{peak} = \sqrt{L_0C}\,f_t(\psi) \tag{9}$$

$$f_t(\psi) \equiv \left(\frac{1}{\sqrt{1-\psi^2}}\sin^{-1}(\sqrt{1-\psi^2})\right) \tag{10}$$

where $f_J(\psi)$ and $f_t(\psi)$ are designated the 'normalized peak functions'. These two relations are shown as functions of ψ in figure 3 with exact values of the functions at $\psi = 1$ highlighted. The slope of the current in the first segment of the discharge is then simply J_{peak}/t_{peak}:

$$J(t)\big|_0^{t_{peak}} = \frac{V_0}{L_0}\frac{f_J(\psi)}{f_t(\psi)}t. \tag{11}$$

In the next segment, our assumption of a close to critically damped waveform is important in determining the correct

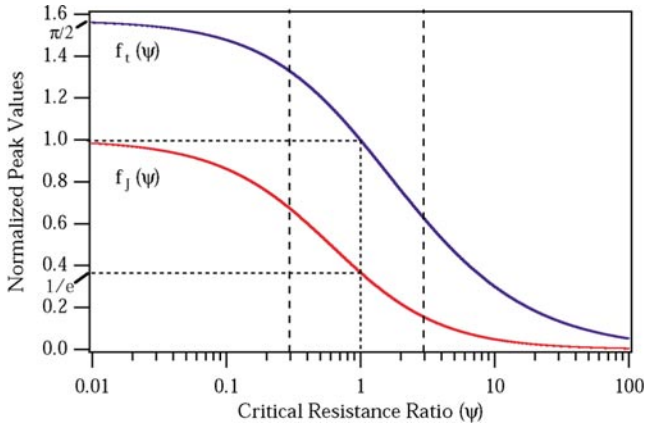

Figure 3. Plot of the normalized peak functions, $f_J(\psi)$ and $f_t(\psi)$, against the critical resistance ratio, ψ. Values of the functions at $\psi = 1$ are shown by horizontal broken lines. The range of ψ of interest to this study is $0.3 \leqslant \psi \leqslant 3$ as shown by the vertical broken lines.

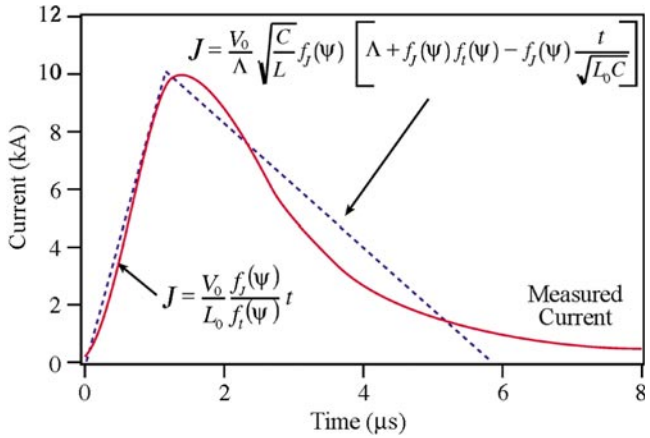

Figure 4. Variable element model for the current of a GFPPT discharge compared to a measured current trace from PT9: 4 J/pulse, 2.0 μg argon, 130 μF, and $1'' \times 1''$ electrodes. (L_0 = 10 nH, C = 130 μF, and V_0 = 242 V.)

slope of the current waveform approximation. For the critically damped case, the slope is related to the increasing inductance and exponentially decaying nature of the actual current waveform. In this case we will assume that the final slope is related to the total change in inductance, ΔL, by a factor Λ,

$$\Lambda \equiv \frac{L_f}{L_0} = 1 + \frac{\Delta L}{L_0} \tag{12}$$

where L_f is the final inductance of the effective discharge circuit when the current sheet has reached the end of the electrodes, $L_f = L'\ell_{electrodes}$. The second segment of the current waveform is then given by

$$J(t)|_{t_{peak}}^{t_{final}} = \frac{V_0}{\Lambda}\sqrt{\frac{C}{L_0}} f_J(\psi) \times \left[\Lambda + f_J(\psi) f_t(\psi) - f_J(\psi)\frac{t}{\sqrt{L_0 C}}\right]. \tag{13}$$

The entire model for the current is shown with a measured current waveform from the PT9 PPT (described in section 3) in figure 4 using the corresponding measured parameters (L_0 = 10 nH, C = 130 μF, and V_0 = 242 V.) The approximate value of the inductance change, $\Lambda \approx 1.5$, is found by assuming that the current sheet reaches the end of the electrodes when the capacitor is fully drained. The model is shown to be in general agreement with this current trace and the thruster parameters assuming $\psi \approx 1$.

As long as the effective resistance of the circuit does not change significantly during the discharge, i.e. ψ is constant, the integral of J^2 can be evaluated in a straightforward manner:

$$\int_0^{t_{final}} J^2 \,\mathrm{d}t = \frac{2}{3} E \sqrt{\frac{C}{L_0}} \left[f_J^2(\psi) f_t(\psi) + f_J(\psi)\Lambda\right]. \tag{14}$$

Using approximations to $f_J(\psi)$ and $f_t(\psi)$ for $0.1 < \psi < 10$ to estimate the normalized peak functions for $0.3 \leqslant \psi \leqslant 3$, we have

$$\int_0^{t_{final}} J^2 \,\mathrm{d}t = \frac{2}{3} E \sqrt{\frac{C}{L_0}} \left[\frac{\pi}{2} \mathrm{e}^{-\sqrt{6\psi}} + \Lambda \,\mathrm{e}^{-\sqrt{\psi}}\right]. \tag{15}$$

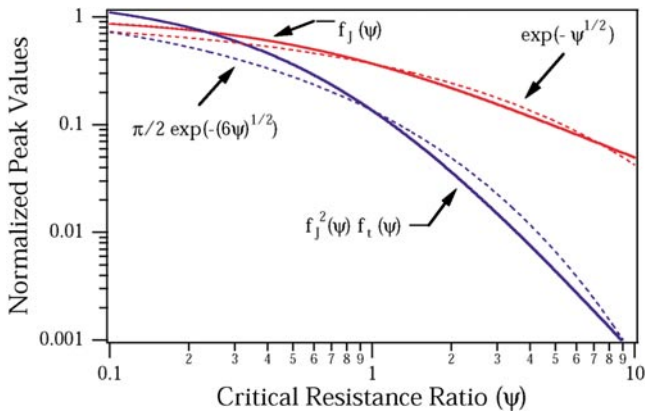

Figure 5. Approximations (broken curves) to the normalized peak functions $f_J(\psi)$ and $f_J^2(\psi)$ (full curves).

These approximations are shown in figure 5 to be in good order-of-magnitude agreement with the actual values of the normalized peak functions over the intended range of ψ, especially near $\psi = 1$ where our study is focused. Now using this approximation to determine the impulse, we integrate the momentum equation (equation (3)) to obtain the impulse bit, I_{bit}:

$$I_{bit} = \int_0^{t_{final}} \left[\frac{\mathrm{d}}{\mathrm{d}t}(mu)\right] \mathrm{d}t \tag{16}$$

$$= \frac{1}{2} L' \int_0^{t_{final}} J^2 \,\mathrm{d}t \tag{17}$$

$$= \frac{1}{3} E L' \sqrt{\frac{C}{L_0}} \left[\frac{\pi}{2} \mathrm{e}^{-\sqrt{6\psi}} + \Lambda \,\mathrm{e}^{-\sqrt{\psi}}\right]. \tag{18}$$

Note that the *impulse* does not depend on how the propellant was accumulated. We have made no assumptions regarding the mass distribution within the thruster since we are, so far, dealing only with the exit conditions of the discharge. The position history of the current sheet during the discharge, however, cannot be found without knowing the mass distribution. Although the mass distribution does not determine the impulse, it does determine the *energy* required to accelerate the entire mass down the length of the electrodes

to the exit velocity. This in turn affects the thrust efficiency (defined in (22)) as discussed in [13, 19].

There is still one unknown in equation (18): Λ. To determine Λ we add another constraint: the integral of the current over the discharge time simply equals the initial charge on the capacitor, CV_0. This implies that the capacitor voltage at the end of the discharge is zero and that current no longer flows after t_{final}. Once again, we use equations (11) and (13) to model the discharge current waveform and we find that

$$\Lambda = 2 - f_t(\psi) f_J(\psi). \tag{19}$$

Using this relation, we can simplify the expression for the impulse bit,

$$I_{bit} = \frac{2}{3} E L' \sqrt{\frac{C}{L_0}} \mathrm{e}^{-\sqrt{\psi}}. \tag{20}$$

Using the standard definition of the exhaust velocity

$$u_e \equiv \frac{I_{bit}}{m_{bit}} \tag{21}$$

the thrust efficiency, η_t, defined as

$$\eta_t \equiv \frac{I_{bit}^2}{2 m_{bit} E} \tag{22}$$

becomes

$$\eta_t = \frac{1}{3} L' \sqrt{\frac{C}{L_0}} u_e \, \mathrm{e}^{-\sqrt{\psi}} \tag{23}$$

$$= \frac{u_e}{U} \mathrm{e}^{-\sqrt{\psi}} \tag{24}$$

$$\propto \chi \tag{25}$$

where we have introduced the EM-PPT characteristic velocity, U,

$$U \equiv \frac{3}{L'} \sqrt{\frac{L_0}{C}} \tag{26}$$

and the EM-PPT performance scaling number, χ,

$$\chi \equiv \frac{u_e}{U}. \tag{27}$$

Note that if the total resistance in the circuit (including the plasma) is zero ($\psi = 0$), then the maximum efficiency is reached when $u_e = U$ and $\chi = 1$. In this respect, the EM-PPT characteristic velocity is the maximum obtainable exhaust velocity if there are no resistive losses in the complete discharge circuit. If $\psi > 0$, the maximum exhaust velocity can be larger than U, and χ can be greater than unity. The EM-PPT characteristic velocity is only a function of the driving circuit and the electrode geometry, making it *uniquely determined for each PPT design*.

The performance scaling number is a non-dimensional parameter that can be used to display performance measurements and check the validity of the scaling law expressed by equation (25). Similarly, the non-dimensional impulse-to-energy ratio,

$$(I/E)^* = \frac{I_{bit}}{E} U \tag{28}$$

is a useful non-dimensional parameter to compare thruster designs. Both the performance scaling number and the non-dimensional impulse-to-energy ratio will be used in the following section to examine measured scaling trends.

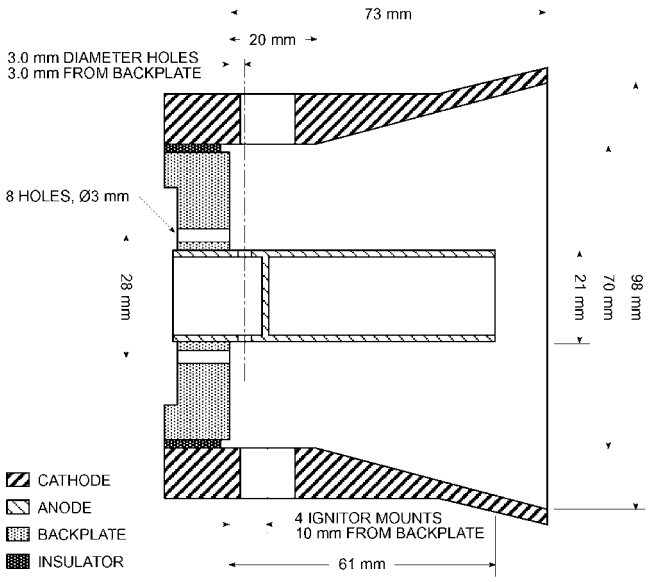

Figure 6. Schematic diagram of PT5.

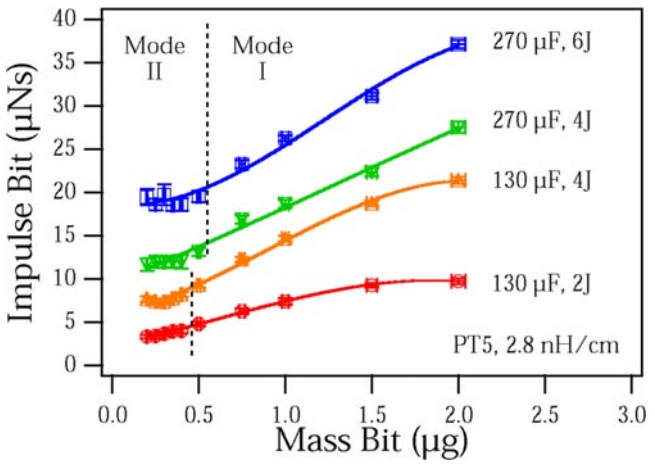

Figure 7. Measured impulse bit of PT5 with argon propellant at two capacitance and two energy values. Mode I and Mode II are separated by the vertical broken lines and are described in section 3.1.

3. Measured performance of GFPPTs

In order to determine if the performance scaling relations developed in the previous section are valid, two GFPPT designs were tested over a wide range of operational conditions. The two thrusters, PT5 and PT9, were developed specifically to observe the performance scaling trends using various mass bit, energy, capacitance, and inductance-per-unit-length values. PT5 was designed with a modular energy storage bank and coaxial electrodes in order to measure the effects of changing the capacitance and energy while keeping the inductance per unit length constant. PT9 was designed with modular parallel-plate electrodes in order to measure the effects of changing the inductance per unit length while keeping the capacitance and energy constant. Both designs were tested over a range of argon propellant mass bit values spanning an order of magnitude.

The performance measurement techniques and associated facilities are described in detail in [3, 20] and the thrusters themselves have been described in [3, 12]. The impulse measurements are made using an impulsive swinging-gate

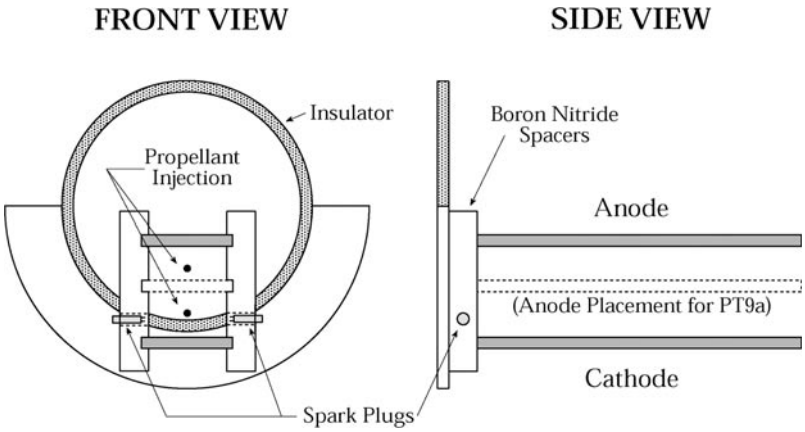

Figure 8. Schematic diagram of PT9b with $1'' \times 1''$ electrodes as well as the anode placement for PT9a. PT9c uses $\frac{1}{2}''$ wide electrodes with the same vertical $1''$ placement as PT9b.

thrust stand where the impulse is found from the time history of the oscillating response of the thrust stand using a laser interferometer [20] or a radio-frequency proximeter [19] yielding measurement errors below 2% as described in these references. The performance of PT5 is presented in detail in [3], and the performance of PT9, with and without sidewalls, is presented in [11]. A short summary of these measurements will be provided in this section. Finally, the GFPPT characteristic velocity needed to normalize the measured performance data will be evaluated for each thruster design.

3.1. Performance of PT5

The PT5 coaxial thruster, shown schematically in figure 6, was designed with a modular energy storage device using either a 130 or 270 μF capacitor bank to determine the effects of capacitance and energy on performance. As described in [3], PT5 showed two modes of operation depending on the mass bit. Figure 7 shows impulse bit measurements over a wide range of mass bit, capacitance, and energy levels. The cut-off between Mode I and Mode II operation is near 0.5 μg/pulse and slightly decreases with decreasing capacitance. Mode I operation occurs for mass bit values above the cut-off and is characterized by an impulse bit and an impulse-to-energy ratio that increase monotonically with the mass bit. This leads to a relatively constant thrust efficiency in this mode of operation. In Mode II operation, the impulse bit and impulse-to-energy ratio are largely independent of the mass bit, leading to an efficiency that varies linearly with exhaust velocity as expected by the model developed in the previous section. Possible explanations of the dependences in Mode I operation are given in the appendix.

3.2. Performance of PT9

PT9 uses variable width ($1''$ and $\frac{1}{2}''$) parallel-plate electrodes at two separation distances, ($1''$ and $\frac{1}{2}''$) in order to vary the inductance per unit length as shown in figure 8 and discussed in more detail in [12]. Three configurations were tested (a, b, and c) to measure the effect of increasing the inductance per unit length while keeping the capacitance and energy constant near 130 μF and 4 J, respectively. The smallest value of the inductance per unit length (configuration a) was designed to be similar to the L' value of PT5.

In [12], Pyrex sidewalls were used with PT9 to contain the propellant injected prior to the discharge. In [11] it was shown that the performance of PT9 improved *without* sidewalls, especially at the lowest mass bit values where the exhaust velocity is the highest. Although the sidewalls help to contain the propellant before the discharge and focus the exhaust stream, they also can significantly retard any moving ions that collide with them and recombine on the surface. Ion diffusion to the insulator walls has previously been suspected as a significant loss mechanism in magnetic shock tubes [21] and plasma guns [22]. Regardless of the physical nature of the 'drag', the negative effect of having any extra surface area exposed to the discharge was quite apparent. For this reason it was decided that the performance of PT9 was best measured again *without* sidewalls.

The performance of PT9 over a wide range of mass bit values and three values of inductance per unit length without sidewalls was shown in [11]. A graph of the impulse bit as a function of mass bit is shown here, in figure 9, for convenience. In all the measurements, a 130 μF capacitor bank was used to keep the charging time requirements to a minimum with as little propellant escaping beyond the electrode volume as possible. The capacitors were charged up to approximately 250 V for each of the six pulses in a burst. The maximum performance level measured with PT9 was attained at the highest inductance-per-unit-length configuration, which yielded a thrust efficiency of 25% at an I_{sp} of 8000 s and an efficiency of 15% measured near 5000 s. In general, the efficiency of PT9 varies linearly with the exhaust velocity as predicted by the model described in the previous section. The impulse-to-energy ratio increases almost linearly with increasing inductance per unit length. Both of these trends will be discussed in more detail in the following section.

3.3. EM-PPT characteristic velocity values

The main design parameters for GFPPT hardware are the capacitance, initial inductance, and inductance per unit length. These three parameters can be condensed into a single one that can effectively be used to predict performance: the EM-PPT characteristic velocity, U, defined in equation (26). This characteristic parameter is derived from easily measurable quantities listed in table 1. Note that larger values of U

Table 1. Thruster test configurations with argon propellant at 0.2–2.0 μg/pulse. Because PT5 has slightly flared electrodes the inductance-per-unit-length value, L', shown here is an average value. The inductance-per-unit-length values for PT9 are found using a conformal mapping technique of the electrode geometry as described in [12].

Thruster	Geometry	Capacitances (μF)	L' (nH cm^{-1})	Energy (J)	U (km s^{-1})
PT5					
(a)	Coaxial	130	~2.8	2	94
(b)	Coaxial	130	~2.8	4	94
(c)	Coaxial	270	~2.8	4	65
(d)	Coaxial	270	~2.8	6	65
PT9					
(a)	Parallel plate	130	2.8	4	94
(b)	Parallel plate	130	3.9	4	67
(c)	Parallel plate	130	5.7	4	46

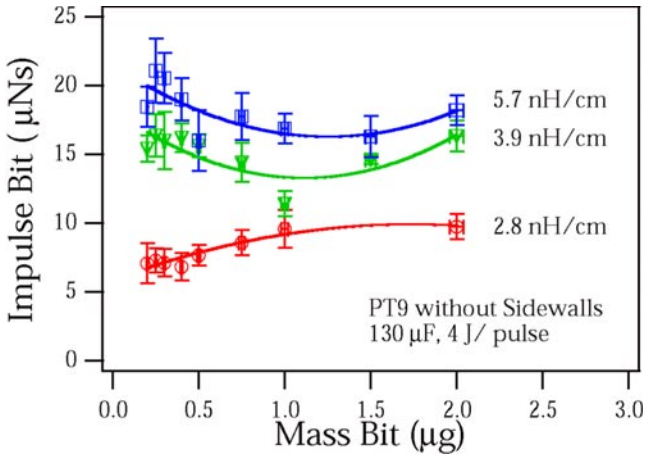

Figure 9. Measured impulse bit of PT9 with argon propellant at three different inductance-per-unit-length values.

correspond to smaller capacitance and inductance-per-unit-length values.

4. Comparison of scaling relations with measurements

Three scaling trends have been predicted by the model developed in section 2:

(1) the impulse bit should scale linearly with the integral of the square of the current,
(2) the impulse-to-energy ratio should be relatively constant over both mass bit and exhaust velocity,
(3) the thrust efficiency should be linearly proportional to the non-dimensional exhaust velocity.

We will now examine these three predictions one at a time.

4.1. Impulse bit scaling with $\int J^2\,\mathrm{d}t$

Figure 10 shows the measured impulse bit as a function of the integral of $J^2(t)$ for both PT5 and PT9. With the open electrode design of PT9, deriving the current from the measured voltage waveform was difficult due to electromagnetic interference (EMI) effects. Consequently, the errors in estimating the current waveform for these cases is large as reflected by the error bars in figure 10. Still, for both thrusters we see a linear trend with $\int J^2\,\mathrm{d}t$ as expected. For the case of PT9, the scatter

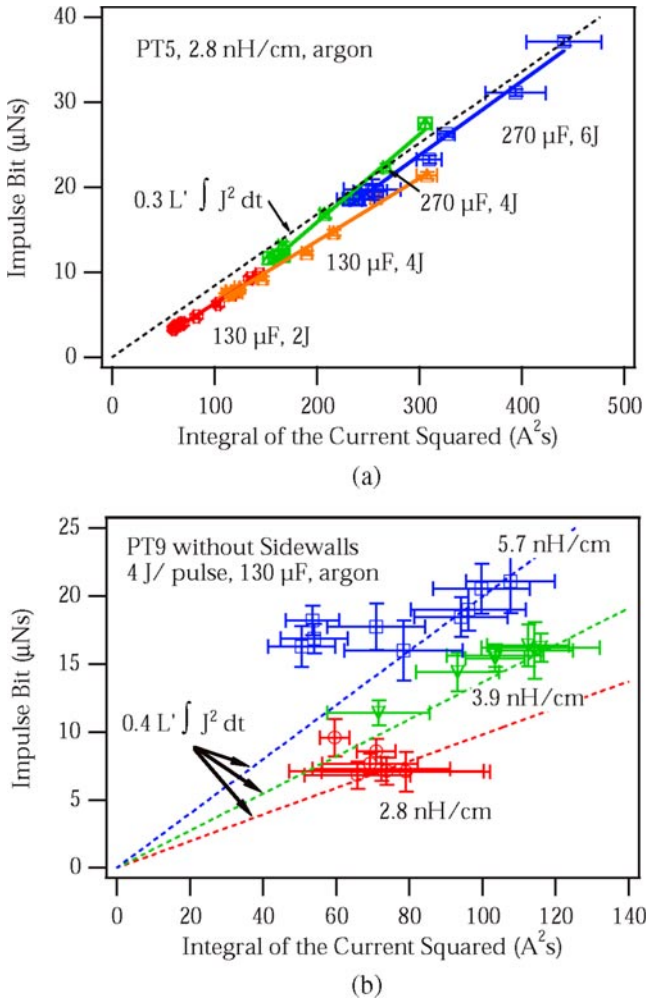

Figure 10. Impulse bit as a function of the integral of the square of the current for both PT5 (a) and PT9 (b) over a wide range of operational conditions.

is most likely due to EMI effects. Also, note that for PT5 the integral of the square of the current and the measured impulse bit both increase by as much as a factor of two for each curve. The integral of J^2 stays relatively fixed for PT9 although the impulse bit increases with increasing inductance per unit length. For PT5, the inductance per unit length does not change and the slope of a line going through the data in each case is very similar, as expected.

From equation (17) the impulse bit should be proportional to $L'/2 \int J^2 \, dt$. The slopes of the lines that fit the measurements, however, are slightly smaller than predicted. This could be due to a number of loss mechanisms that are not accounted for by the model. These potential losses include energy going into unrecoverable plasma internal modes, profile losses due the canting of the current sheet, and the conduction of ions to the cathode creating wall losses as described in section 3.2. Again, although proportionally the impulse bit values are lower than expected, they do scale linearly with the integral of the square of the current.

4.2. Energy-to-impulse ratio scaling with mass bit

Graphs of the impulse as a function of mass bit, with the energy as a varying parameter, for each thruster have already been shown in figures 7 and 9. Normalizing the impulse bit by the discharge energy and the EM-PPT characteristic velocity, U, yields the non-dimensional impulse-to-energy ratio, $(I/E)^*$, as defined in equation (28). This normalization causes all the curves of measured $(I/E)^*$ for all ranges of capacitance, inductance per unit length, and energy to collapse onto a single curve as shown in figure 11. This upholds the validity of the scaling law implicit in equation (28). In general, the trend of the impulse bit scaling with the energy level, the square root of the capacitance, and the inductance per unit length is present throughout the data from both thrusters. At mass bit values below 0.5 μg, both thrusters share a similar value of $(I/E)^*$ near 0.2, but PT5 has a larger value than PT9 at higher mass bits in Mode I operation. This trend will be examined in more detail in the appendix. For now it is important to notice that although there is an increase in $(I/E)^*$, it is similar for all four curves related to PT5.

For PT9, the three curves for $(I/E)^*$ are more similar at higher mass bits. The $1'' \times 1''$, 3.9 nH cm^{-1} configuration of PT9b seems to have the highest value at the lower mass bits. This could be due to it having slightly more propellant to accelerate compared to the $\frac{1}{2}''$ wide case of PT9c where more propellant might have escaped before the discharge was initiated. Compared to the $\frac{1}{2}''$ gap of PT9a, PT9b has a smaller electrode surface-to-volume ratio with a $1''$ gap, possibly reducing wall losses. Still, compared to the separated curves of the measured impulse bit in figure 9, the curves of $(I/E)^*$ in figure 11 are very similar.

4.3. Efficiency scaling with χ

Perhaps the most important prediction for the performance scaling of GFPPTs is the linear scaling of the efficiency with the exhaust velocity. This trend was predicted by the model developed in section 2, equation (24). Except for Mode I operation (high mass bit, low exhaust velocity) in PT5, this is generally true from measured performance, as shown in figure 12. These graphs show the combined measurements for all seven configurations of the two GFPPT designs. In figure 12(a), the curves are spread out depending on capacitance, inductance per unit length, and energy as the thrust efficiency is plotted against the measured exhaust velocity. In figure 12(b), the thrust efficiency is plotted against the performance scaling number, χ. Much of the data can be

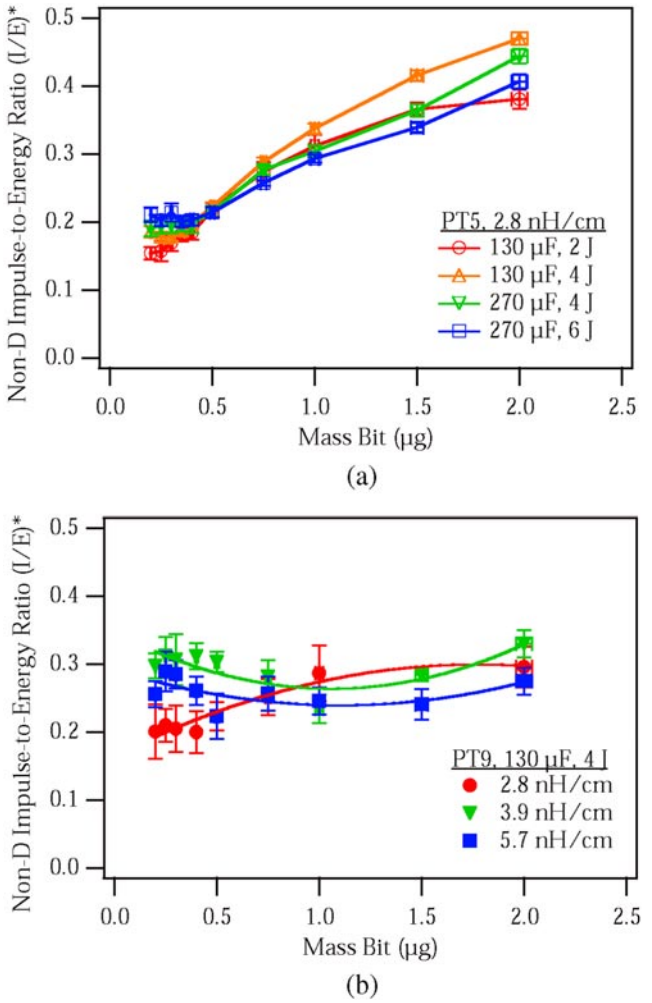

Figure 11. Non-dimensional impulse-to-energy ratio as a function of mass bit for both PT5 (a) and PT9 (b).

seen to collapse within 10% of a *single line*, $\eta_t = \chi/8$. This upholds the validity of the scaling model derived in section 2 over a wide range of measured parameters. For the low-energy GFPPTs tested here, the efficiency is almost always related to the performance scaling number.

The linear coefficient of the line fit to the performance data, 1/8, corresponds to a critical resistance ratio of about four (see equation (25)). The largest deviations from this linear trend are at high mass bit values in PT5 Mode I operation and some slight deviations in PT9 at higher mass bit values. In the appendix we present four potential explanations for these deviations and argue that the plasma resistance could be decreasing at the higher mass bits. Smaller values of the effective plasma resistance reduce ψ and, hence, are likely to increase η_t.

5. Conclusions and implications

5.1. Summary and conclusions

An analytical model was used to derive performance scaling relations for EM-PPTs. A fundamental parameter to these relations is the EM-PPT performance scaling number, defined as the ratio of the exhaust velocity to the EM-PPT characteristic velocity. The relations were tested with a GFPPT experimental

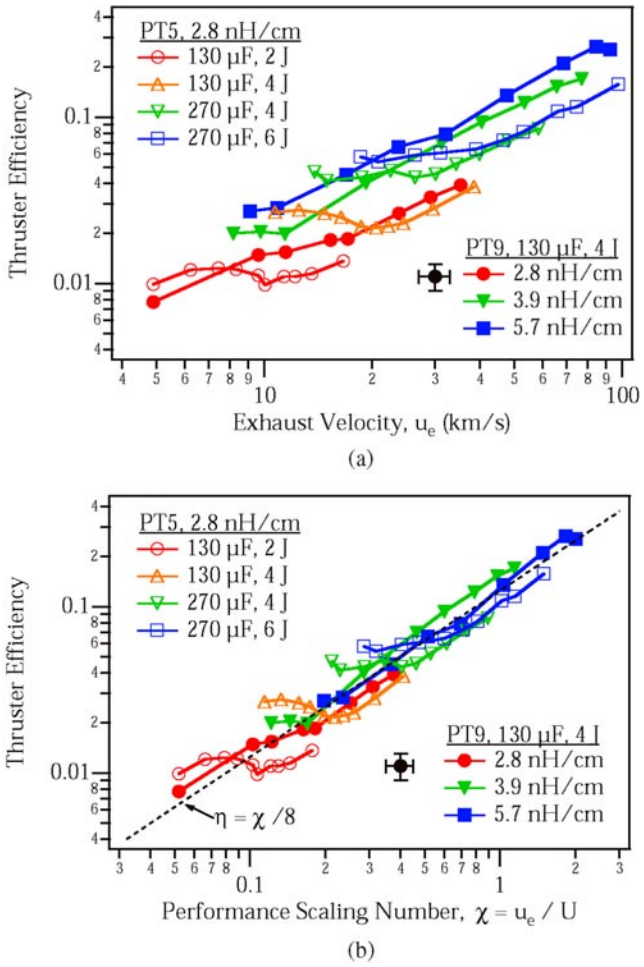

Figure 12. Thrust efficiency as a function of exhaust velocity and the performance scaling parameter, $\chi = u_e/U$, with a sample error bar shown near the legends. Using the performance scaling number allows almost all the data to fall close to one line, $\eta_t = \chi/8$.

data base over a range of 70 different operational conditions. The following conclusions can be drawn from this study.

- The thrust efficiency is directly proportional to the EM-PPT performance scaling number for the conditions tested here,

$$\eta_t \propto \chi = \frac{u_e}{U} = \frac{1}{3} L' \sqrt{\frac{C}{L_0}} u_e. \qquad (29)$$

- For the low-energy GFPPTs studied here, the effective plasma resistance seems to be significant and plays an important role in determining performance.
- All measured performance data (η, u_e, and I_{bit}/E) can be made to collapse onto single, universal curves when non-dimensionalized according to the predicted scaling laws.

Although these scaling laws were tested over a wide range of parameters, it remains interesting to explore their validity at higher discharge energies, with different propellant types as well as with APPTs operating in the electromagnetic acceleration mode. Another remaining question is the explicit relation between the operating conditions and the plasma resistance, which impacts the model through the parameter ψ.

5.2. Practical implications

The identification and validation of these scaling laws have several practical implications. A scaling relation in the form of equation (29) is already in the form $\eta(I_{sp})$ (where $I_{sp} = u_e g_0$ is the specific impulse and g_0 is the acceleration of gravity at sea level) which is commonly used in mission analysis to study the suitability of a particular thruster type for a given mission. Such use of the scaling relations also allows the specification of the design parameters of the thruster as a function of the mission requirements.

Another practical value of having validated scaling relations in hand is their usefulness in predicting the performance of a prototypical thruster using the measured performance of another that differs from the former by having different values for one or more of the parameters in equation (29).

The most significant implication is perhaps the identification of the design parameters and dependences that are important for designing and testing thrusters as well as the suggestion of future research directions for improving their performance. Improving the performance often means raising the efficiency at a given specific impulse (or exhaust velocity). This is also equivalent to raising the impulse-to-energy (or thrust-to-power) ratio for a given I_{sp}. In this context the scaling relation in equation (29) tells us that this can be achieved by increasing the inductance per unit length and capacitance, and decreasing the initial inductance and plasma resistivity. While the practical prescriptions for effecting these changes and the related limitations are not the subject of the paper, (they have been discussed elsewhere [3, 12, 13, 19]), the following brief comments can be made. Increasing the inductance per unit length is easier to achieve with a parallel-plate configuration, but such a geometry has some disadvantages related to propellant containment and wall losses [12]. Increasing the capacitance carries a mass penalty due to increased capacitor mass as well as a propellant utilization penalty due to longer capacitor charging time [12] (which can lead to propellant loss between consecutive pulses). Decreasing the initial inductance is of course always beneficial and a significant reduction in this parameter has already been achieved with the present generation of devices where L_0 is at or below 10 nH. Finally, decreasing the plasma resistivity is the least explored and understood route to improving performance and should represent the primary focus of plasma physics studies of the device.

Acknowledgments

Research supported by the Air Force Office of Scientific Research, grant number: F49620-98-1-0119 and the Plasma Science and Technology Program at the Princeton Plasma Physics Laboratory.

Appendix. Possible explanations for the dependences in Mode I

As seen in almost all the comparisons between measurements and models, the largest discrepancies occur for PT5 in Mode I operation. In this mode the efficiency does not decrease

monotonically with exhaust velocity and the impulse-to-energy ratio increases with increasing mass bit. We can think of four different explanations for the higher than predicted performance: electrothermal energy recovery, finite electrode length effects, increased profile or sweeping efficiency, or a decrease in the effective plasma resistance at higher mass bit values. The real explanation could be a combination of these ideas, which we will now discuss consecutively.

A.1. Electrothermal energy recovery

At the higher mass bit values of Mode I, the number density and pressure are higher and the mean free path is correspondingly lower compared to Mode II operation. Consequently the likelihood of electrothermal energy recovery into thrust is higher for Mode I. The scaling relations expected for a thruster where electrothermal acceleration is dominant, however, are quite different (see, for example, [23]). In this case, the impulse bit is expected to scale with the *square root* of the discharge-energy-to-mass-bit ratio and not to depend directly on capacitance or inductance change. This is a result of the energy deposited in the plasma being proportional to the integral of RJ^2. The *efficiency* of a pure electrothermal accelerator is expected to be constant over wide range of energy, exhaust velocity, and mass bit values. While the efficiency for PT5 is indeed independent of mass bit and exhaust velocity at high mass bit values (i.e. Mode I), it does show a dependence on energy.

Other evidence against this explanation is the relation between the impulse bit and integral of the square of the current, as shown in figure 10. For an electrothermal thruster, the exhaust velocity and hence the impulse bit should scale as the square root of the integral of the square of the current. Clearly this is not the case with the measured trends, having more of a linear character, as would be expected for electromagnetic acceleration. Moreover, even at mass bit values that clearly fall into Mode I operation, the impulse-to-energy ratio was found to be constant over a wide range of energy values as described in [3]. This is characteristic of an electromagnetic accelerator, not an electrothermal one. Therefore, although some electrothermal energy may well be recovered in these discharges, the amount is believed to be minor and not enough to explain Mode I operation.

A.2. Finite electrode length effects

In Mode I operation, the discharge may not reach the end of the electrodes by the time the capacitor is fully drained. If there is a uniform propellant distribution before the pulse, the current sheet would run into a large amount of unaccelerated propellant after the Lorentz force has vanished. This would impose significant drag on the sheet, however the impulse bit would not be affected. With the amount of mass increasing at the same rate as the velocity is decreasing, the impulse bit is constant but the efficiency steadily *decreases*. This is, however, contrary to the observed trend.

Instead, if there is an exponential propellant distribution, the efficiency would be highest when the greatest amount of energy in the capacitor is transferred to the discharge. For the smaller mass bits, the current sheet may run to the end of the electrodes well before the capacitor is fully drained, reducing the efficiency. We would expect that as the velocity continues to increase and the electrode length is fixed, the efficiency would decrease as the duration for which the current sheet stays in contact with the electrodes decreases. Once again, this explanation does not match well the observed performance trends.

A.3. Increased sweeping and/or profile efficiency

The sweeping efficiency (the effectiveness of the current sheet in picking up propellant as it moves down the electrodes) and associated profile losses are important aspects of PPTs [7]. Since these have not been quantified directly in our experiments, it is difficult to determine if they are responsible for the higher than expected performance. In previous studies of current sheet structure in argon discharges it has been noticed that the sweeping efficiency increases with increasing current rise rates [7, 24]. An empirical rule of thumb is that 10^{12} A s^{-1} cm^{-1} over the span of the current sheet is required for 100% sweeping efficiency [7]. Most of the low-energy GFPPT discharges presented here fall *just below* this 10^{12} A s^{-1} cm^{-1} cut-off. As seen in figure 10 the current does indeed increase as the mass bit value increases, which could imply that the sweeping efficiency is improving. Still, as shown in section 2, the *impulse* should not depend on how the mass was swept up. In other words, although the thrust efficiency should be sensitive to the sweeping efficiency, the impulse-to-energy ratio should not. In addition, both [24] and [25] showed that the sweeping efficiency *decreased* for higher mass bit values.

As to the possibility of a profile efficiency increase in Mode I operation, once again the literature points towards the opposite of the trends we observed with mass bit and pressure. Using an inverse z-pinch device, Johansson [25] found that the tilting of the current sheet (which causes profile losses) *increased* for higher mass bit values. Although the profile efficiency should effect both the thrust efficiency and the impulse-to-energy ratio, the existing models appear to predict the opposite trend. In addition, the GFPPTs used in our study have much shorter electrodes compared to any accelerator where significant tilting and profile losses have been found to occur.

A.4. Decrease in effective plasma resistance

Another possibility is based on the potentially changing value of ψ with the mass bit (which is related to the initial propellant density). As apparent in all the comparisons between predicted and measured performance, as the mass bit increases the measured performance moves closer to values that are predicted by smaller critical resistance ratios. As the initial inductance and capacitance are fixed, this would imply that the effective resistance in the circuit (capacitor internal impedance plus plasma resistance) decreases as the mass bit (and density) increases. Once again we turn to figure 10 and note that the current levels also increase at higher mass bit values. In fact, the mass bit cut-off between a relatively constant integral of J^2 and where the integral values begin to increase agrees well with the transition point found in figure 7. As expected, and found in previous experiments [21, 26], as both the energy and current increase, the effective plasma

resistance drops. In light of the observed trends, a decreasing value of ψ is therefore the most plausible explanation for the observed enhancement of the performance of PT5 in Mode I.

References

[1] Choueiri E Y 1996 Optimization of ablative pulsed plasma thrusters for stationkeeping missions *J. Spacecraft Rockets* **33** 96–100

[2] Burton R L and Turchi P J 1998 Pulsed plasma thruster *J. Propulsion Power* **14** 716–35

[3] Ziemer J K, Choueiri E Y and Birx D 1999 Is the gas-fed PPT an electromagnetic accelerator? An investigation using measured performance *Proc. 35th Joint Propulsion Conf. (Los Angeles, CA, 20–24 June, 1999)* AIAA 99-2289

[4] Jet Propulsion Laboratory 1999 NASA facts: Europa orbiter *Technical Report* NASA

[5] Staehle R L *et al* 1993 Exploration of Pluto *Acta Astronautica* **30** 289–310

[6] Blandino J J and Cassady R J 1998 Propulsion requirements and options for the new millennium interferometer (DS-3) mission *Proc. 34th Joint Propulsion Conf. (Cleveland, OH, 13–15 July, 1998)* AIAA 98-3331.

[7] Jahn R G 1969 *Physics of Electric Propulsion* (New York: McGraw-Hill)

[8] Michels C J, Heighway J E and Johansen A E 1996 Analytical and experimental performance of capacitor powered coaxial plasma guns *AIAA J.* **4** 823–30

[9] Gloersen P, Gorowitz B and Kenney J T 1966 Energy efficiency trends in a coaxial gun plasma engine system *AIAA J.* **4** 436–41

[10] Hart P J 1964 Modified snowplow model for coaxial plasma accelerators *J. Appl. Phys.* **35** 3425–31

[11] Ziemer J K and Choueiri E Y 2000 A characteristic velocity for gas-fed PPT performance scaling *Proc. 36th Joint Propulsion Conf. (Huntsville, AL, 16–19 July, 2000)* AIAA 2000-3432

[12] Ziemer J K, Choueiri E Y and Birx D 1999 Comparing the performance of co-axial and parallel-plate gas-fed PPTs *Proc. 26th Int. Electric Propulsion Conf. (Kitakyushu, Japan, 17–21 October, 1999)* IEPC 99-209

[13] Ziemer J K and Choueiri E Y 1998 Dimensionless performance model for gas-fed pulsed plasma thrusters *Proc. 34th Joint Propulsion Conf. (Cleveland, OH, 13–15 July, 1998)* AIAA 98-3661

[14] Ziemer J K, Markusic T E, Choueiri E Y and Birx D 1998 Effects of ignition on discharge symmetry in gas-fed pulsed plasma thrusters *Proc. 34th Joint Propulsion Conf. (Cleveland, OH, 13–15 July, 1998)* AIAA 98-3803

[15] Keefer D and Rhodes R 1997 Electromagnetic acceleration in pulsed plasma thrusters *Proc. 25th Int. Electric Propulsion Conf. (Cleveland, OH, 24–28 August, 1997)* IEPC 97-035

[16] Andrenucci M, Caprili M and Lazzeretti R 1972 Theoretical performance of pulsed coaxial plasma guns *Technical Report* Universita di Pisa

[17] Mostov P M, Neuringer J L and Rigney D S 1961 Electromagnetic acceleration of a plasma slug *Phys. Fluids* **4** 1097–104

[18] Vargo D J 1964 Electromagnetic acceleration of a variable-mass plasma *Technical Report* TN D-2164, NASA

[19] Ziemer J K 2001 Performance scaling of gas-fed pulsed plasma thrusters *PhD Thesis* MAE Department, Princeton University

[20] Cubbin E A, Ziemer J K, Choueiri E Y and Jahn R G 1997 Laser interferometric measurements of impulsive thrust *Rev. Sci. Instrum.* **68** 2339–46

[21] Keck J 1964 Current speed in a magnetic annular shock tube *Proc. Int. Symp. Plasma Guns, Phys. Fluids (Supplement)* **7** S16–S27

[22] Thom K, Norwood J and Jalufka N 1964 Velocity limitation of a coaxial plasma gun *Proc. Int. Symp. on Plasma Guns, Phys. Fluids (Supplement)* **7** S67–S70

[23] Guman W J 1968 Solid propellant pulsed plasma micro-thruster studies *Proc. 6th Aerospace Sciences Meeting (New York, 22–24 January, 1968)* AIAA 68-85

[24] Jahn R G and von Jaskowsky W 1964 Current distributions in large-radius pinch discharges *AIAA J.* **2** 1749–53

[25] Johansson R B 1965 Current sheet tilt in a radial magnetic shock tube *Phys. Fluids* **8** 866–71

[26] Aronowitz L and Duclos D P 1963 Characteristics of the pinch discharge in a pulsed plasma accelerator *Electric Propulsion Development (Progress in Astronautics and Rocketry)* vol 9, ed E Stuhlinger (New York: Academic)